Supplement of

New insights into uncertainties in Antarctic elevation change estimates by comparing radar and laser altimetry

Maria T. Kappelsberger[1], Johan Nilsson[2,3], Martin Horwath[1], Veit Helm[4], and Alex S. Gardner[2]

[1]Chair of Geodetic Earth System Research, TUD Dresden University of Technology, Dresden, Germany
[2]Jet Propulsion Laboratory, California Institute of Technology, Pasadena, USA
[3]Department of Earth Sciences, Uppsala University, Uppsala, Sweden
[4]Alfred-Wegener-Institut Helmholtz-Zentrum für Polar- und Meeresforschung, Bremerhaven, Germany

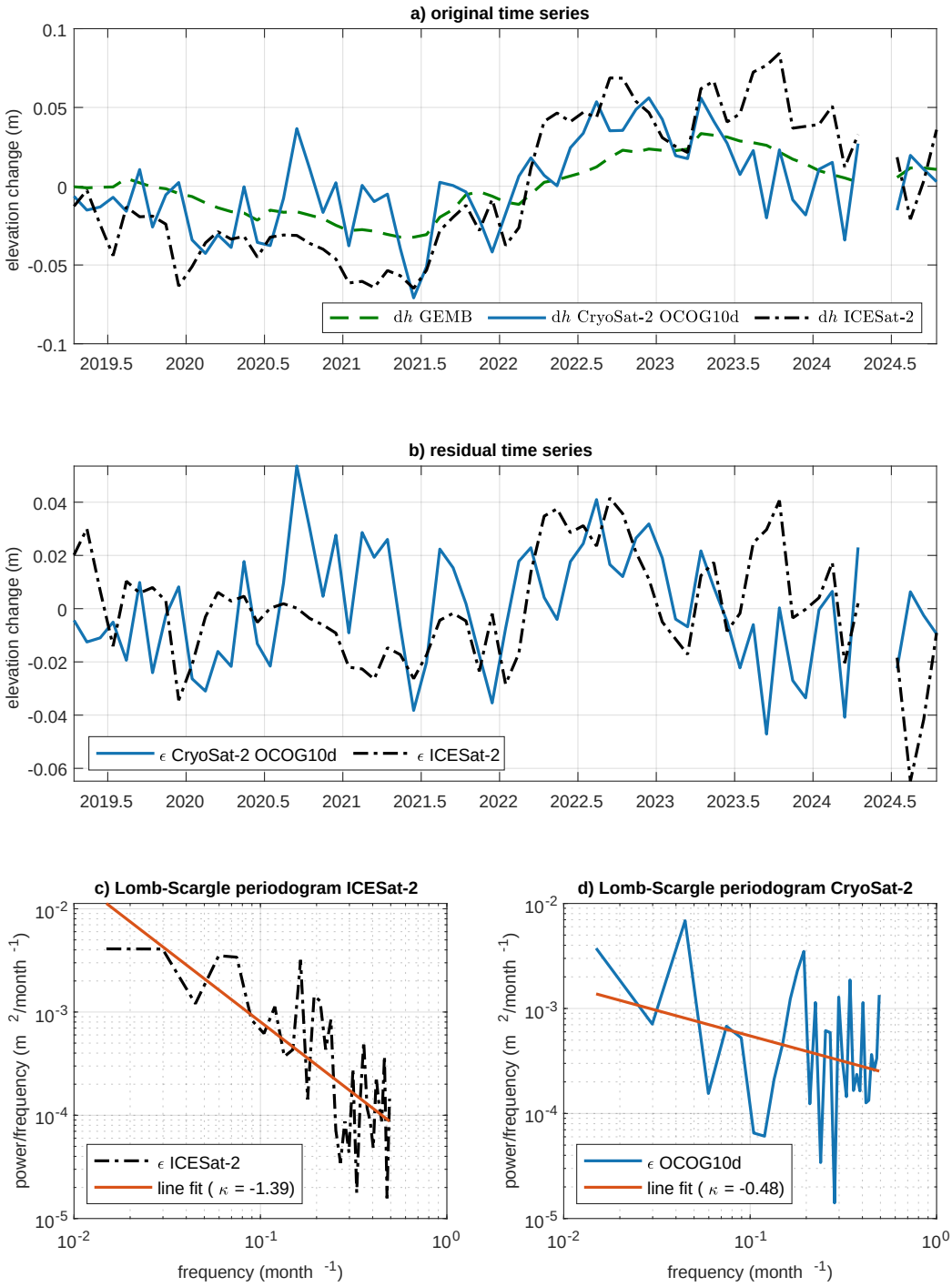

Figure S1. (a, b) Time series and (c, d) power spectral densities for an example grid cell at $x = 1410\,\mathrm{km}$ and $y = -850\,\mathrm{km}$ in the C'-D basin. (a) The original time series of elevation change for GEMB, CryoSat-2 OCOG10d and ICESat-2. (b) The residual time series of elevation change for CryoSat-2 OCOG10d and ICESat-2 and (c, d) their respective power spectral densities, including the fitted lines.

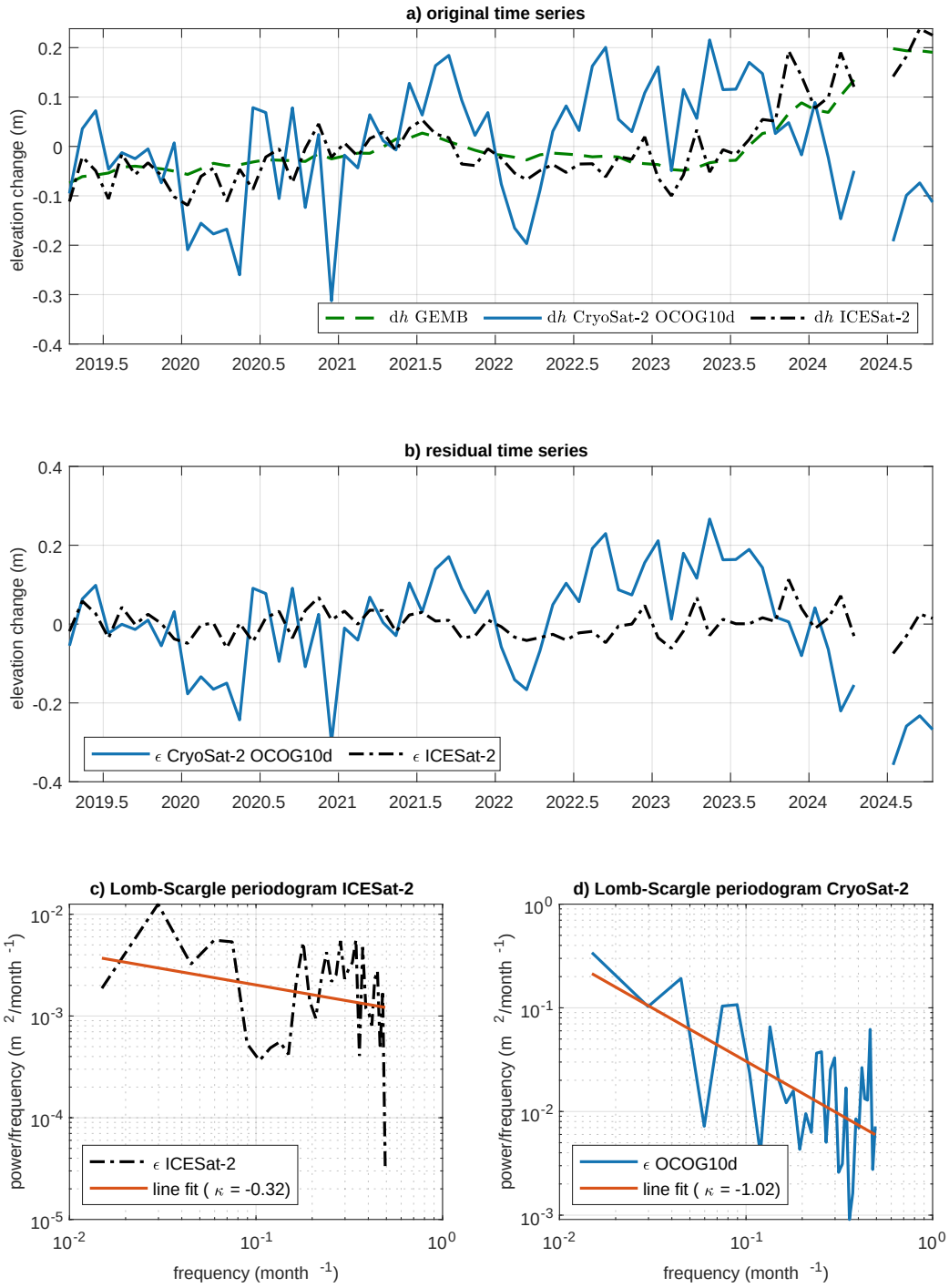

Figure S2. (a, b) Time series and (c, d) power spectral densities for an example grid cell at $x = -350\,\mathrm{km}$ and $y = 820\,\mathrm{km}$ in the J"-K basin. (a) The original time series of elevation change for GEMB, CryoSat-2 OCOG10d and ICESat-2. (b) The residual time series of elevation change for CryoSat-2 OCOG10d and ICESat-2 and (c, d) their respective power spectral densities, including the fitted lines.

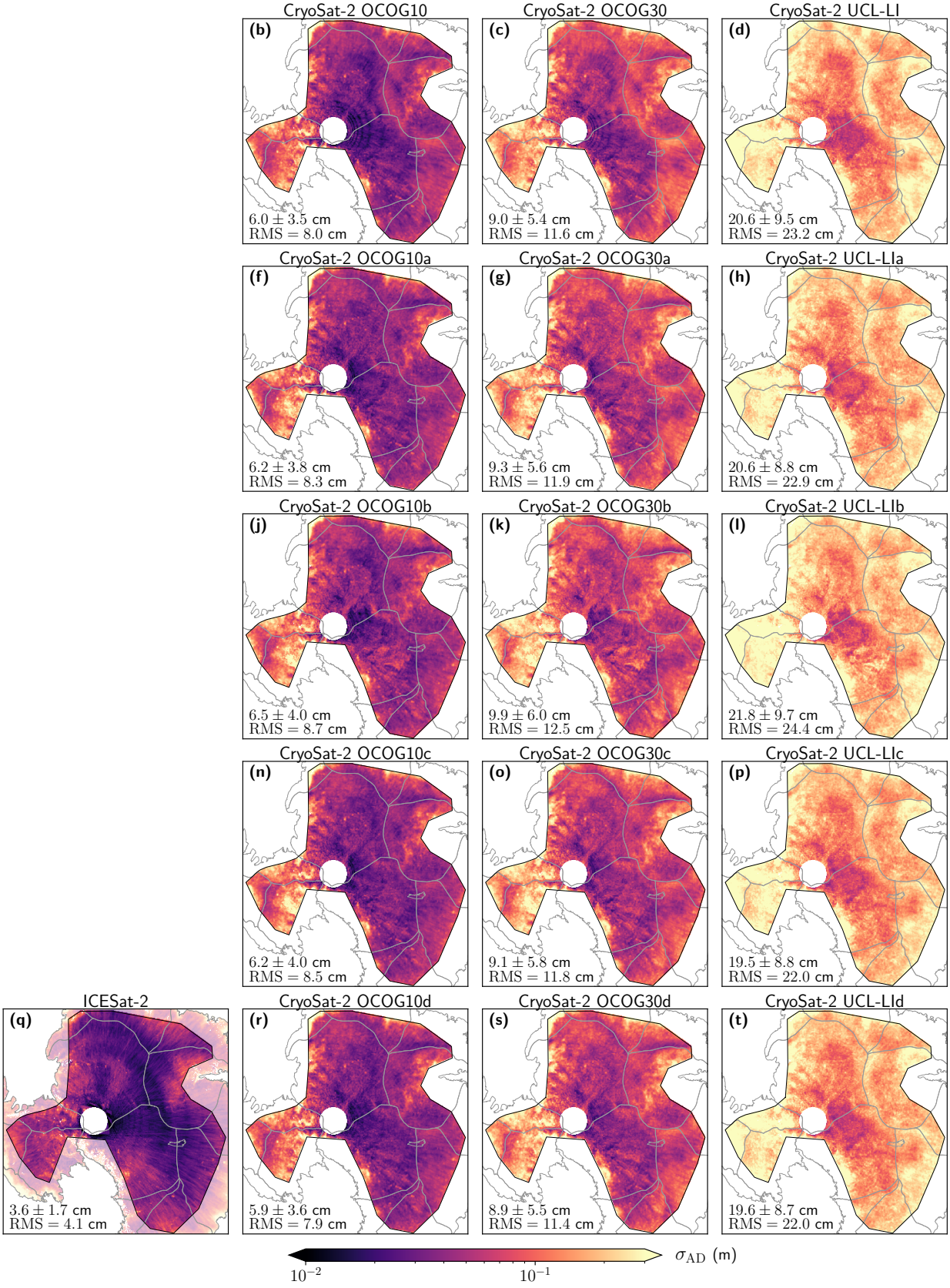

Figure S3. Precision (σ_{AD}) of all 16 altimetry data sets derived in this study for April 2019 to October 2024. The mean ± SD (standard deviation) and RMS (root mean square) for the entire LRM zone are stated in the lower left corner. In this figure and all subsequent ones, the SD is calculated as 1.253 times the mean absolute deviation to ensure robustness against outliers.

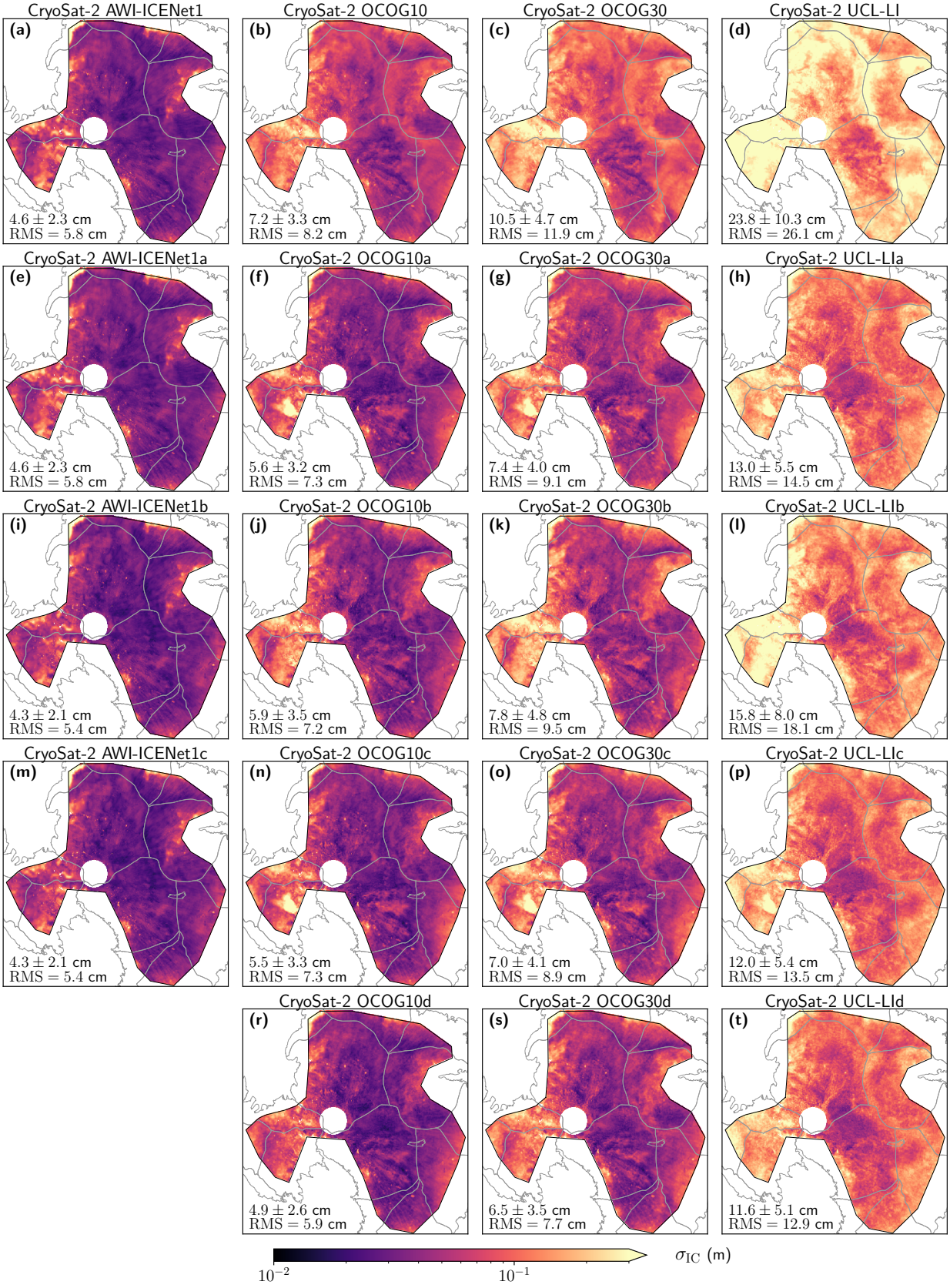

Figure S4. Accuracy (σ_{IC}) of all 19 CryoSat-2 altimetry data sets for April 2019 to October 2024. The mean ± SD and RMS for the entire LRM zone are stated in the lower left corner.

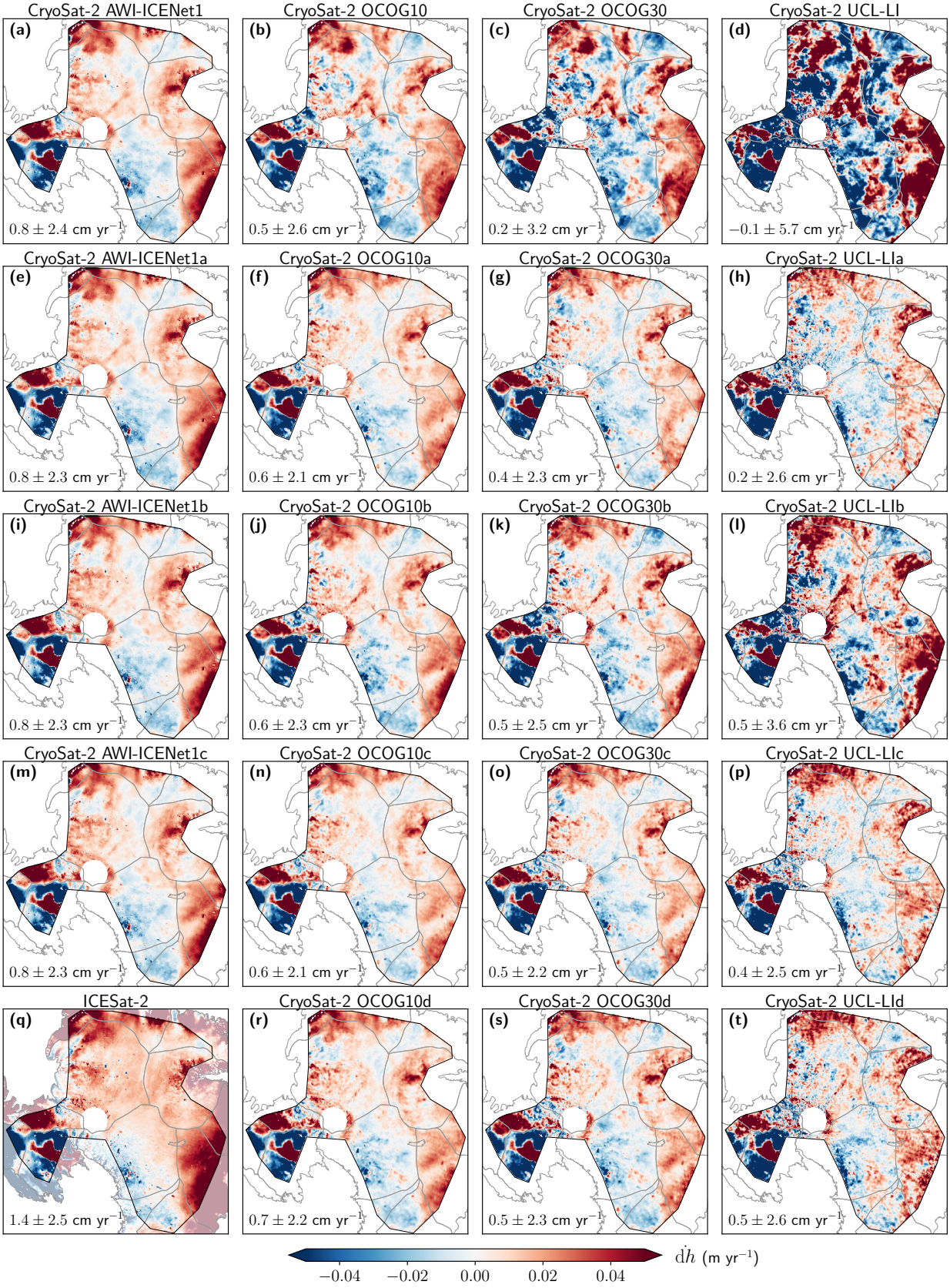

Figure S5. Height change trends ($\dot{h}$) of all 20 altimetry data sets for April 2019 to October 2024. The mean ± SD for the entire LRM zone are stated in the lower left corner.

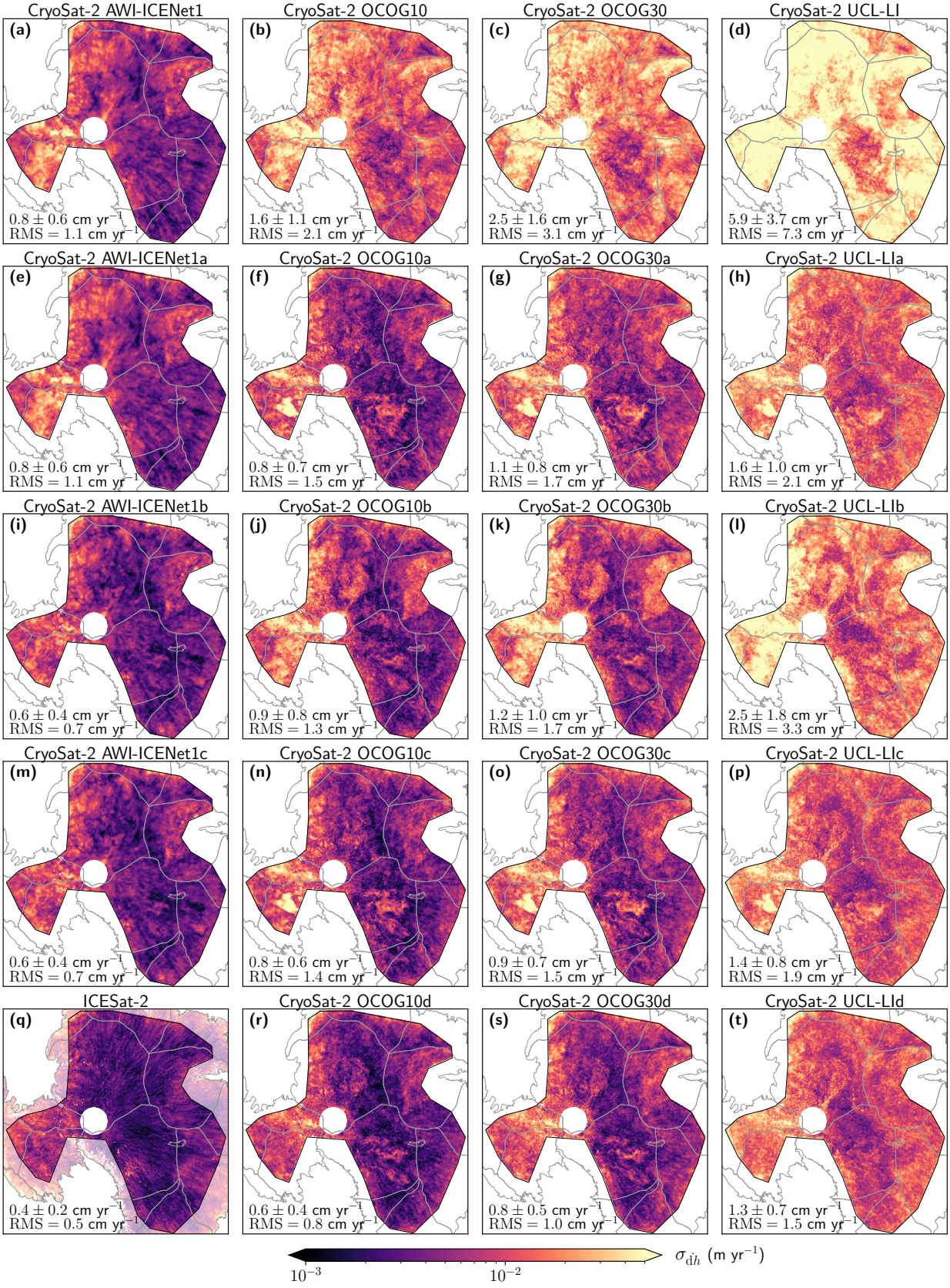

Figure S6. Trend uncertainties ($\sigma_{\dot{dh}}$) of all 20 altimetry data sets for April 2019 to October 2024. The mean ± SD and RMS for the entire LRM zone are stated in the lower left corner.

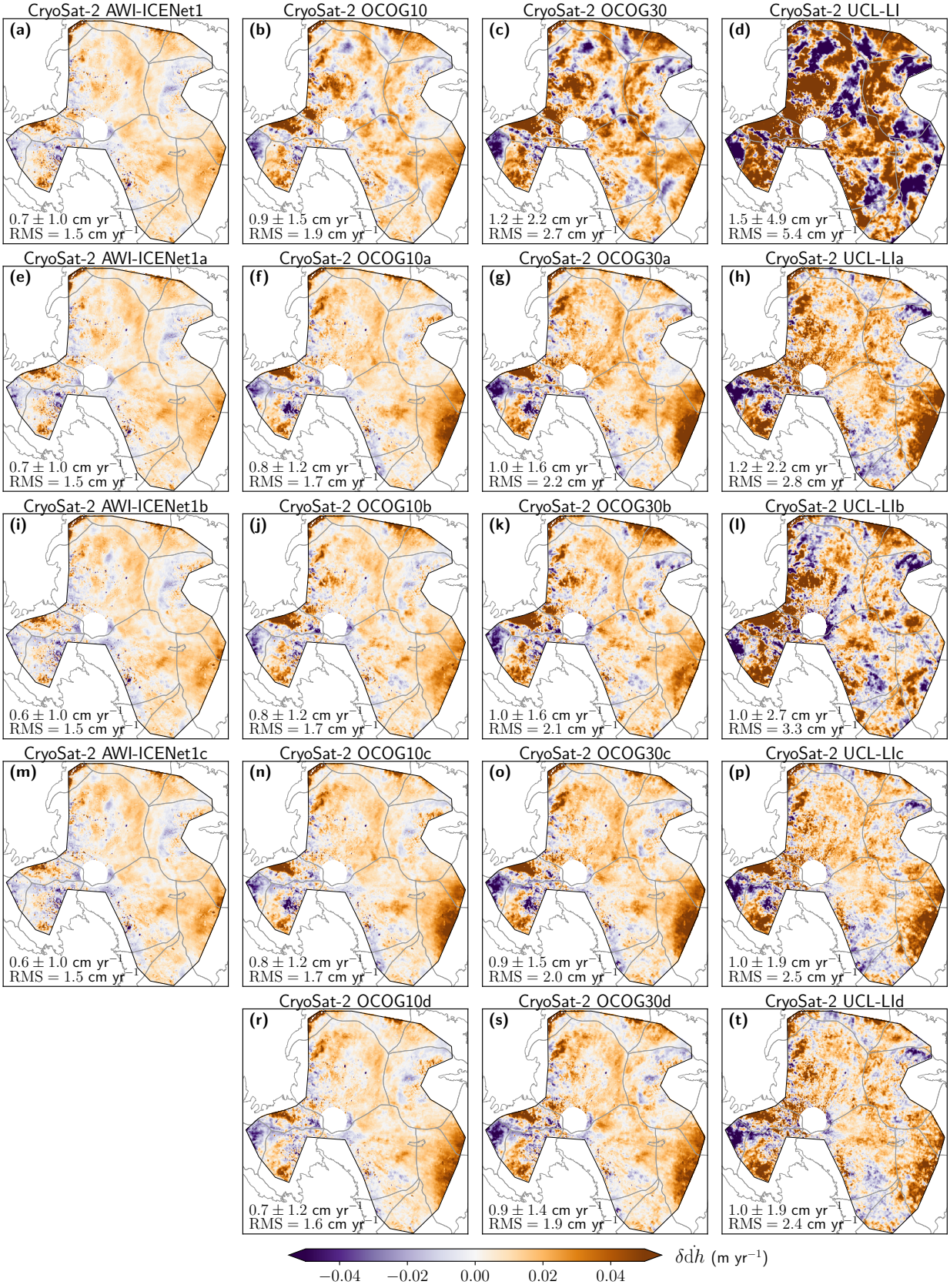

Figure S7. Trend errors ($\delta\dot{h}$) of all 19 CryoSat-2 altimetry data sets for April 2019 to October 2024. The mean ± SD and RMS for the entire LRM zone are stated in the lower left corner.

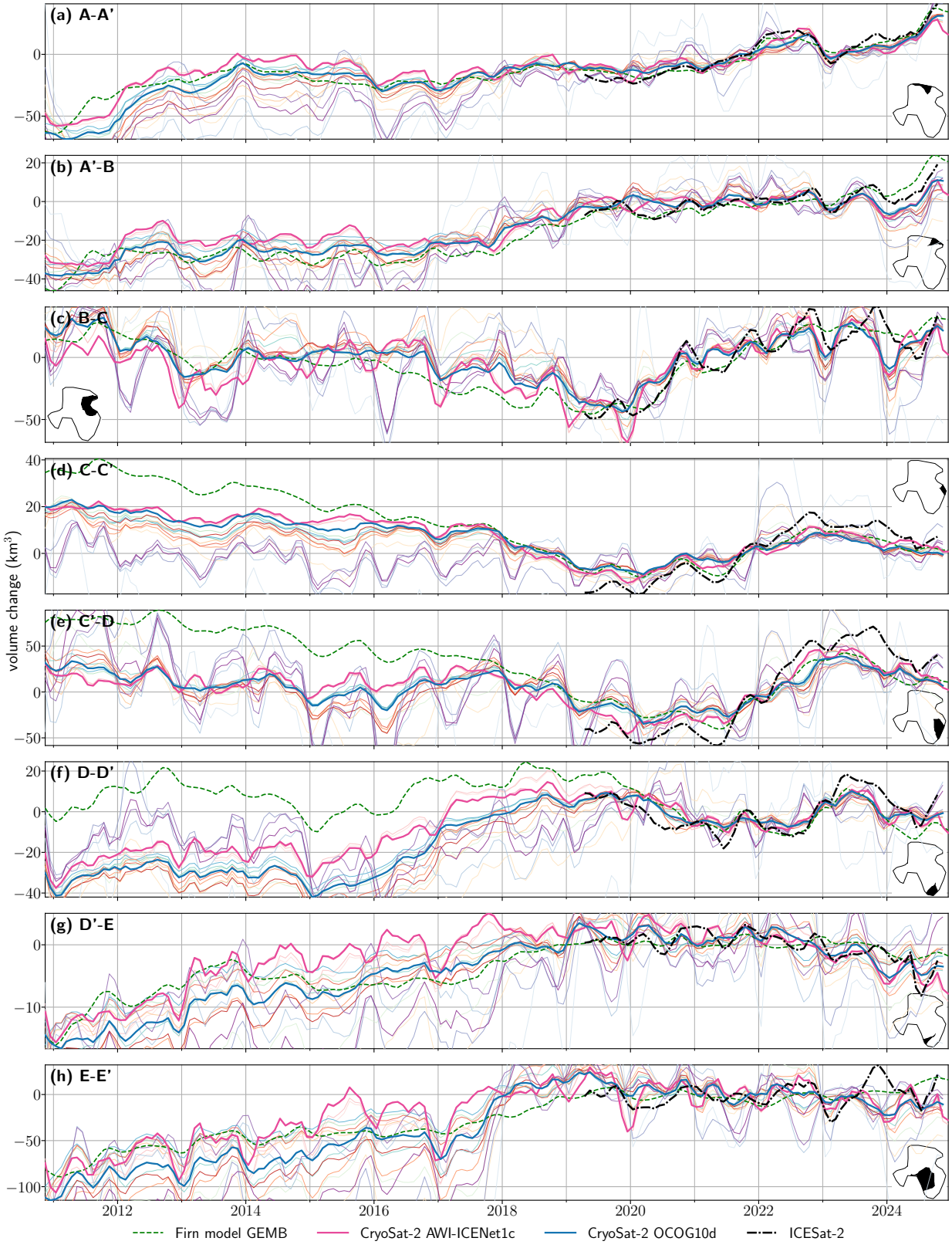

Figure S8. Volume change time series from all data sets for different drainage basin subregions of the LRM zone, shown by the black area on the map in each panel. The thin green-blue, orange-red, purple and pink lines show the CryoSat-2 OCOG10, OCOG30, UCL-LI and AWI-ICENet1 results, respectively. The thicker lines show the best and most discussed results (see legend). Three-month moving averages are applied for visualisation purposes only.

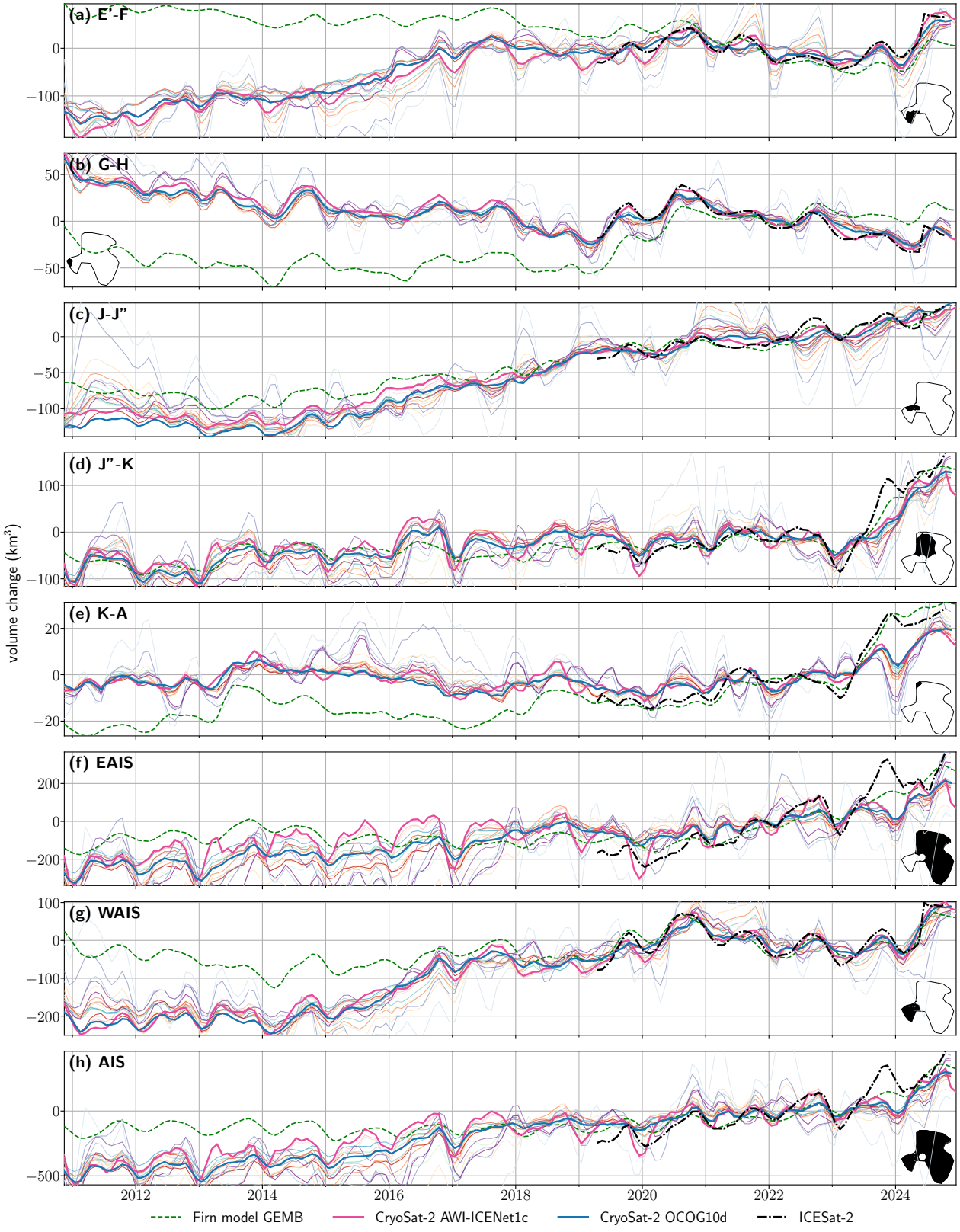

Figure S9. Volume change time series from all data sets for different drainage basin subregions of the LRM zone, shown by the black area on the map in each panel. The thin green-blue, orange-red, purple and pink lines show the CryoSat-2 OCOG10, OCOG30, UCL-LI and AWI-ICENet1 results, respectively. The thicker lines show the best and most discussed results (see legend). Three-month moving averages are applied for visualisation purposes only.

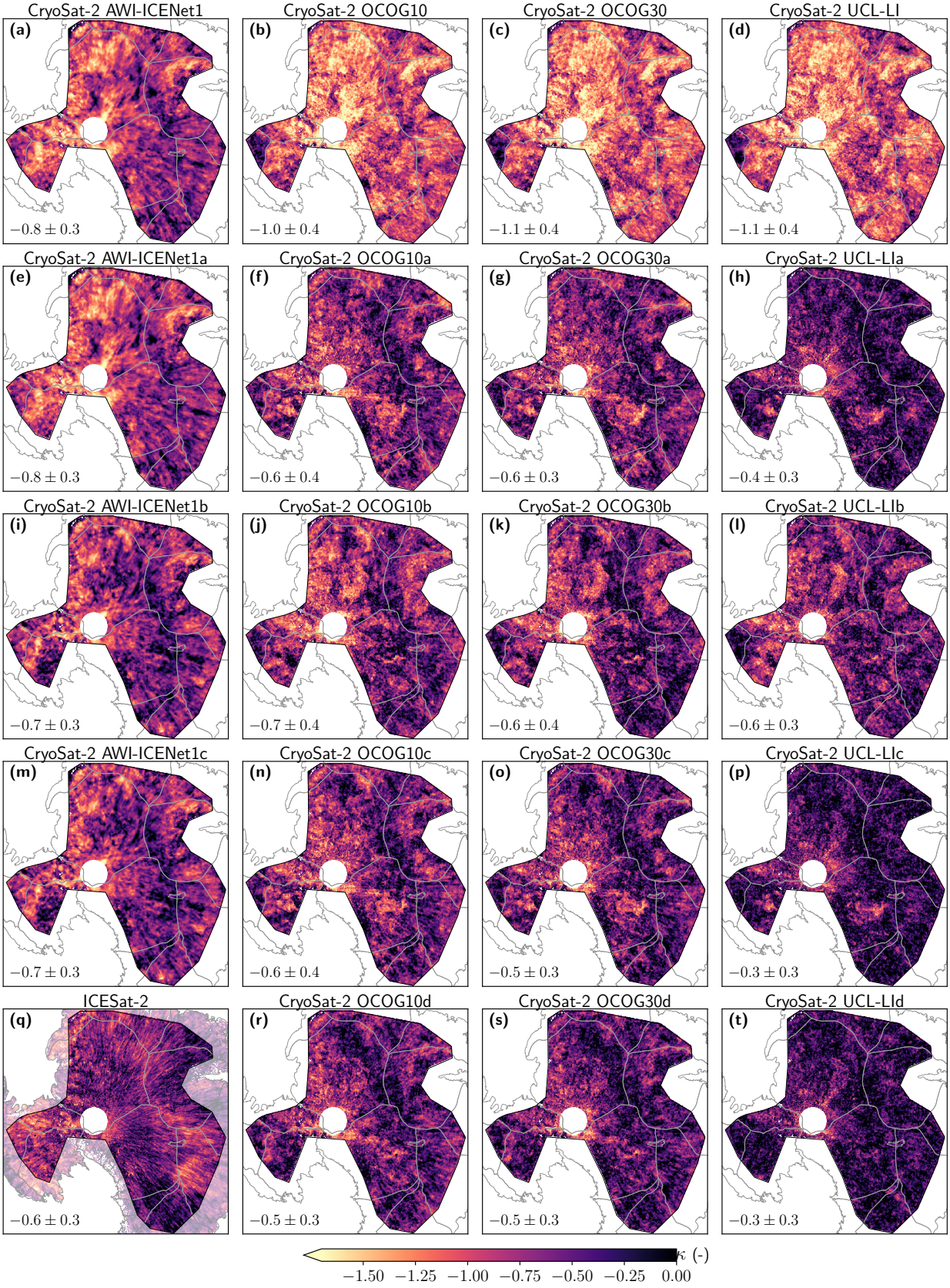

Figure S10. Spectral index (κ) of power-law noise for all 20 altimetry data sets for April 2019 to October 2024. The mean $\pm$ SD for the entire LRM zone are stated in the lower left corner.

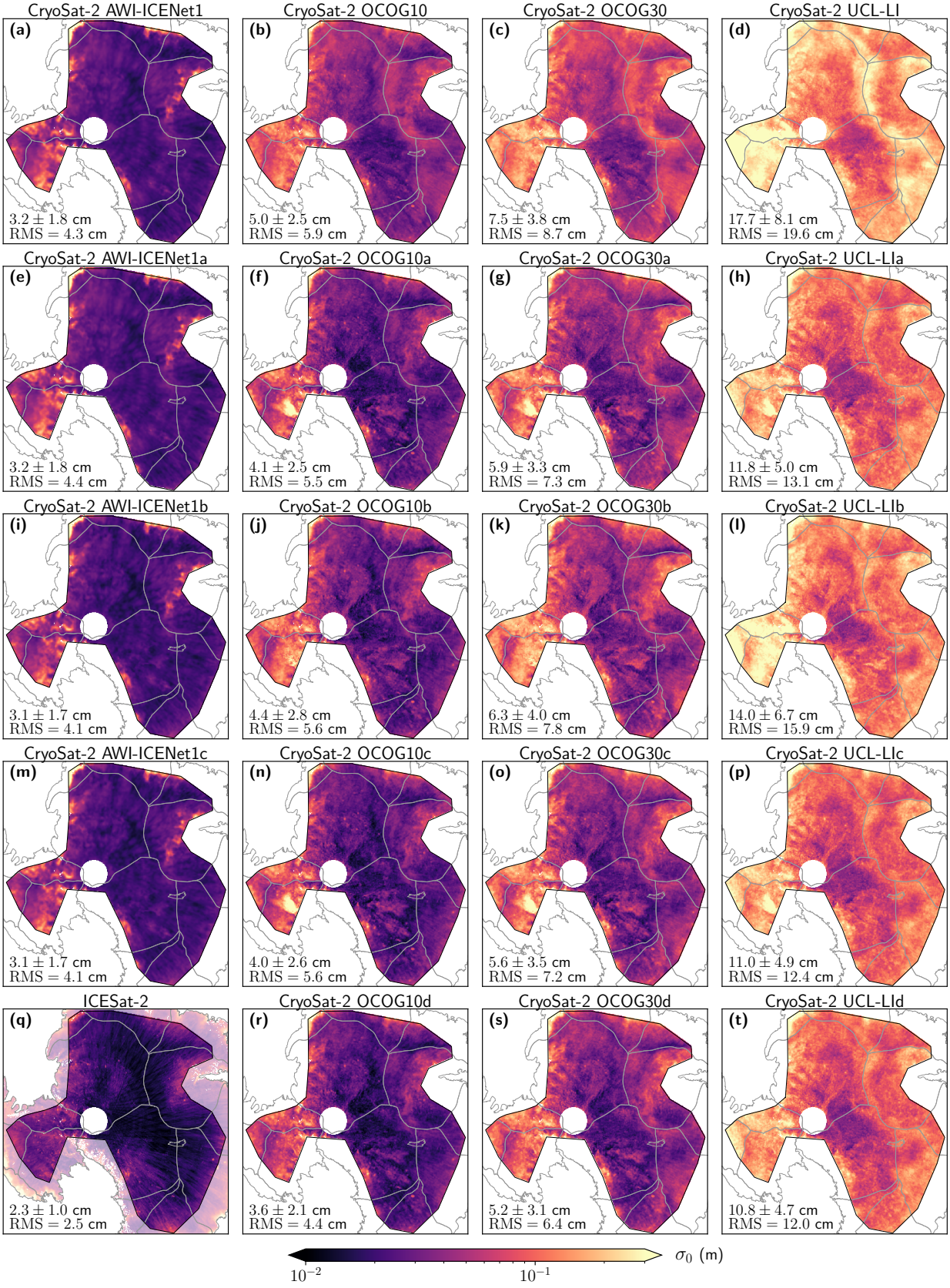

Figure S11. Noise level (σ_0) of all 20 altimetry data sets for April 2019 to October 2024. The mean ± SD and RMS for the entire LRM zone are stated in the lower left corner.

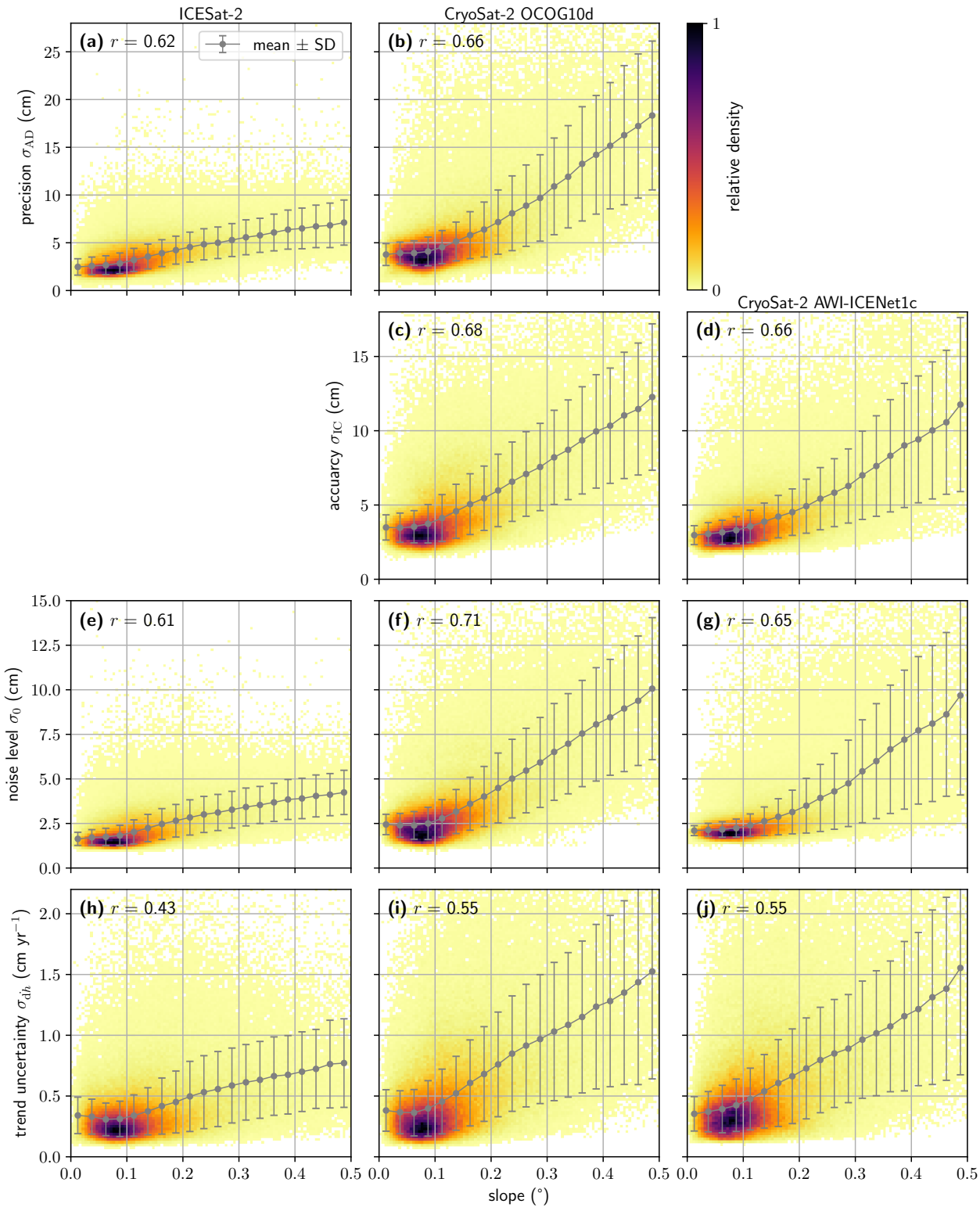

Figure S12. The AIS surface slope plotted against the (a, b) precision (σ_{AD}), (c, d) accuracy (σ_{IC}), (e–g) noise level (σ_0) and (h–j) trend uncertainty ($\sigma_{\dot{dh}}$) for ICESat-2, CryoSat-2 OCOG10d and AWI-ICENet1c shown in the first, second and third columns, respectively. The number of grid cells belonging to one colour-coded pixel is shown from a few (yellow-white) to many (deep purple) cells. Median and MAD values are calculated at 0.025° slope bins, thus 20 intervals between 0.0 and 0.5°. The correlation coefficients between the slope and the uncertainty metrics over the entire LRM zone are stated in the upper left corner.

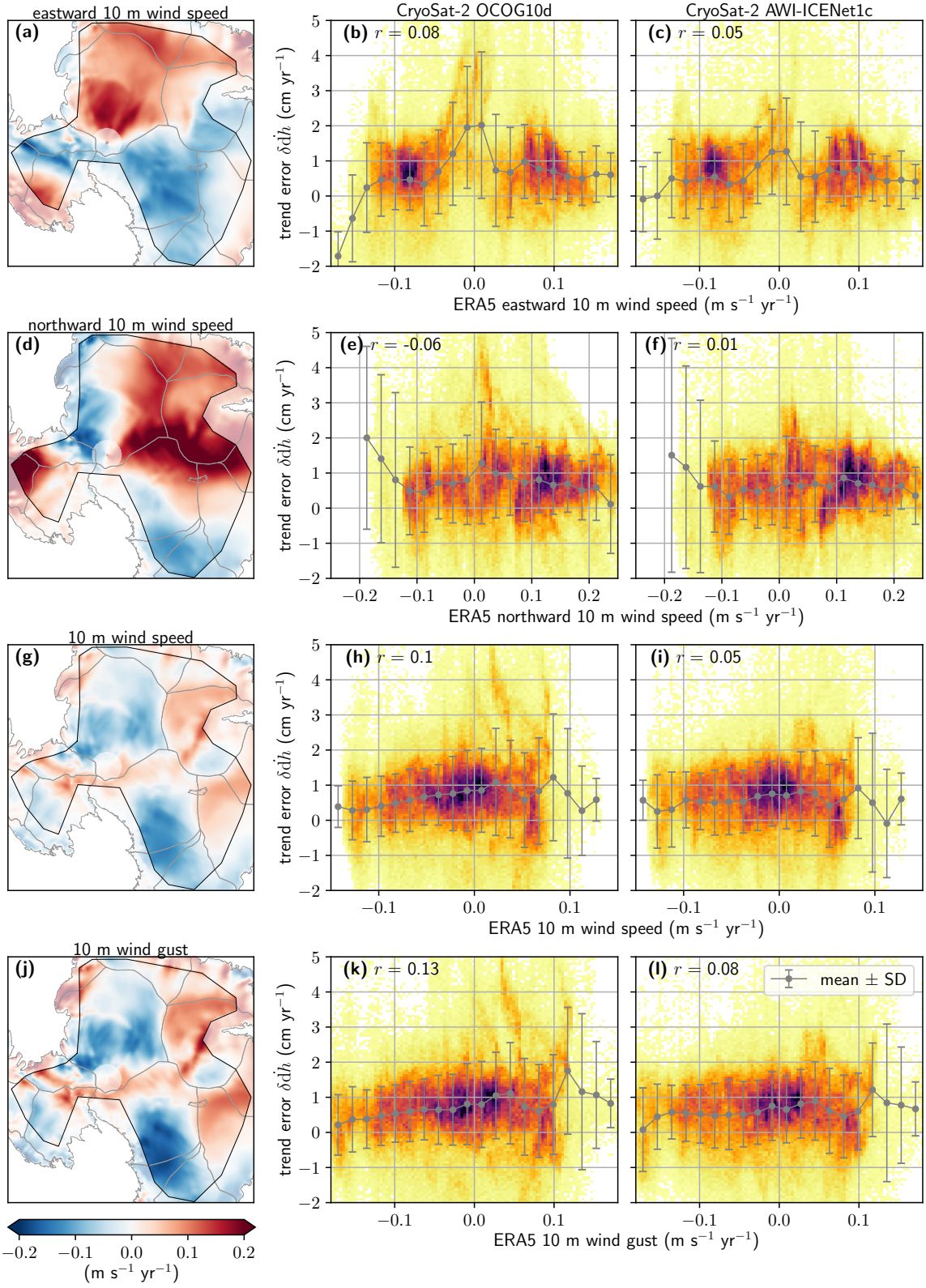

Figure S13. Trends in ERA5 wind speed parameters over the period from April 2019 to October 2024 (first column), and their relationship with the CryoSat-2 trend error ($\delta\dot{h}$) using OCOG10d (second column) and AWI-ICENet1c (third column). The number of grid cells belonging to one colour-coded pixel is shown from a few (yellow-white) to many (deep purple) cells. The correlation coefficients between the ERA5 wind speed trends and $\delta\dot{h}$ over the entire LRM zone are stated in the upper left corner.

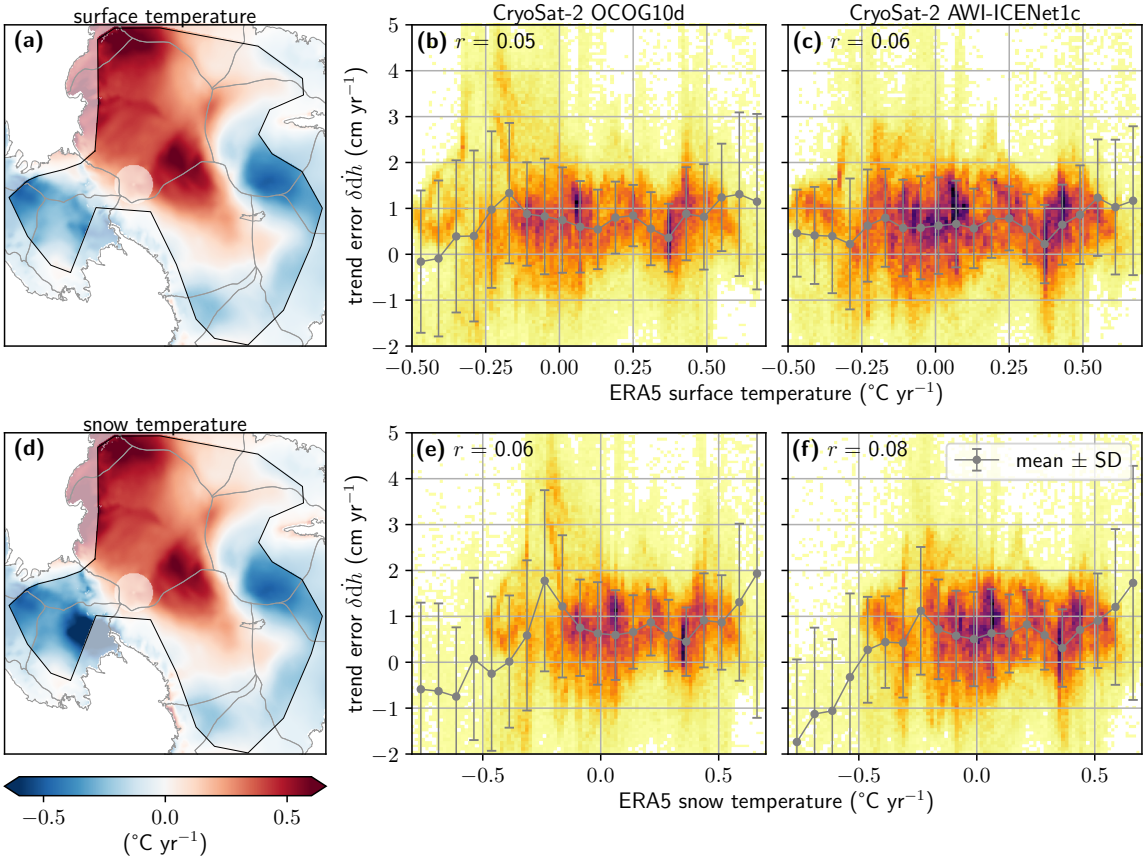

Figure S14. Trends in ERA5 (a) surface and (d) snow temperature over the period from April 2019 to October 2024, and their relationship with the CryoSat-2 trend error ($\delta\dot{dh}$) using OCOG10d (second column) and AWI-ICENet1c (third column). The number of grid cells belonging to one colour-coded pixel is shown from a few (yellow-white) to many (deep purple) cells. The correlation coefficients between the ERA5 temperature trends and $\delta\dot{dh}$ over the entire LRM zone are stated in the upper left corner.

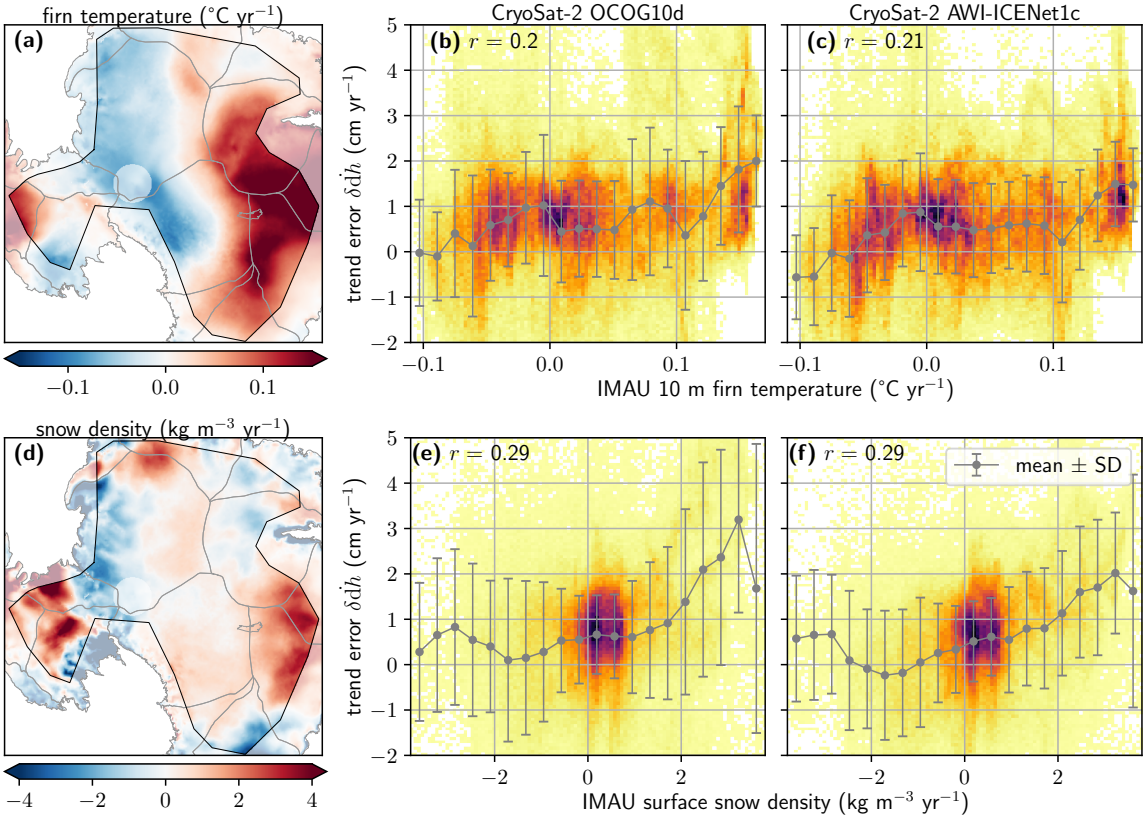

Figure S15. Trends in IMAU (a) firn temperature and (d) surface snow density over the period from April 2019 to December 2023, and their relationship with the CryoSat-2 trend error ($\delta\dot{h}$; also calculated for 2019–2023 to ensure consistency) using OCOG10d (second column) and AWI-ICENet1c (third column). The number of grid cells belonging to one colour-coded pixel is shown from a few (yellow-white) to many (deep purple) cells. The correlation coefficients between the IMAU trends and $\delta\dot{h}$ over the entire LRM zone are stated in the upper left corner.

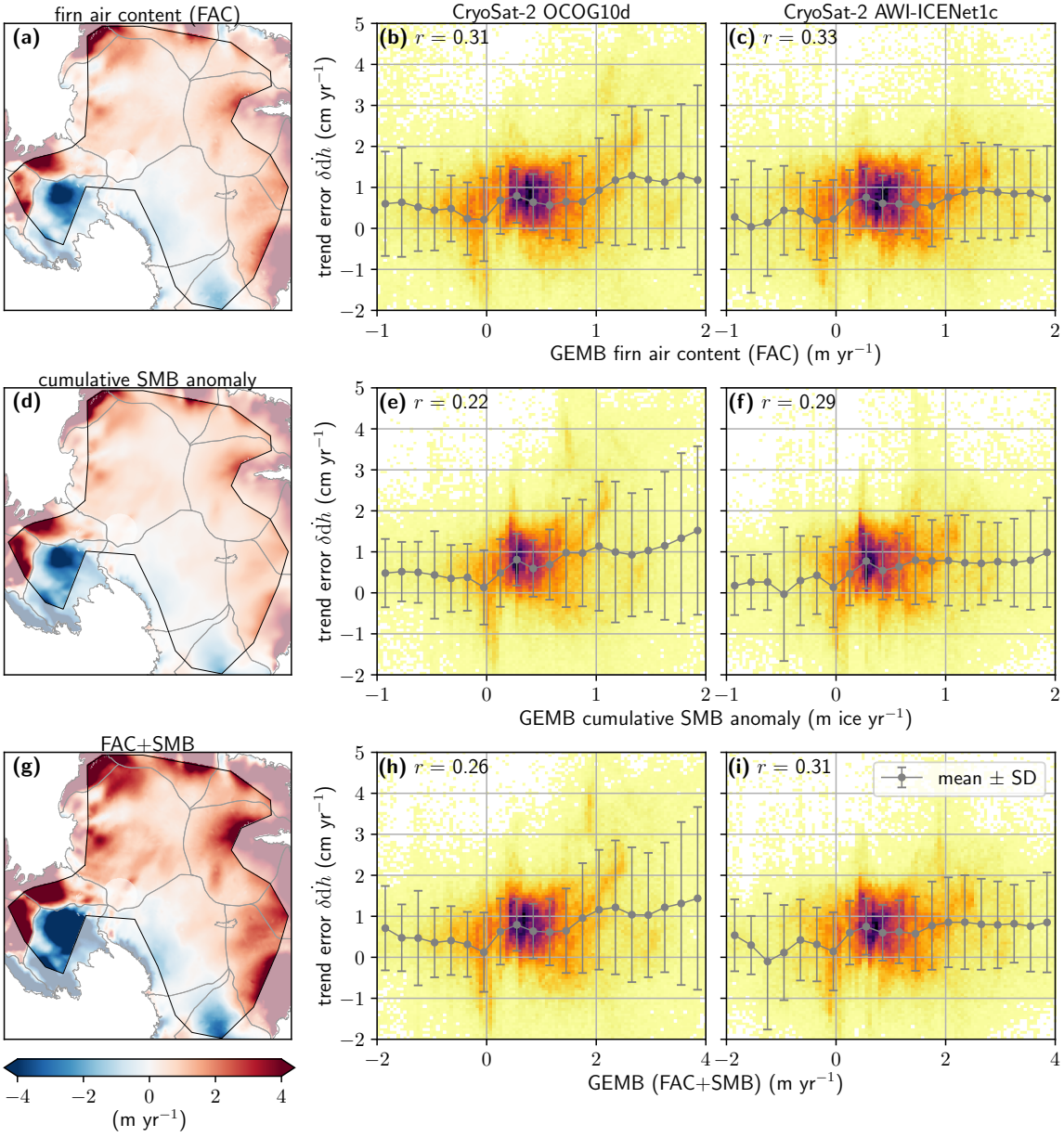

Figure S16. Trends in GEMB height change outputs over the period from April 2019 to October 2024 (first column), and their relationship with the CryoSat-2 trend error ($\delta\dot{d}h$) using OCOG10d (second column) and AWI-ICENet1c (third column). The number of grid cells belonging to one colour-coded pixel is shown from a few (yellow-white) to many (deep purple) cells. The correlation coefficients between the GEMB height trends and $\delta\dot{d}h$ over the entire LRM zone are stated in the upper left corner.

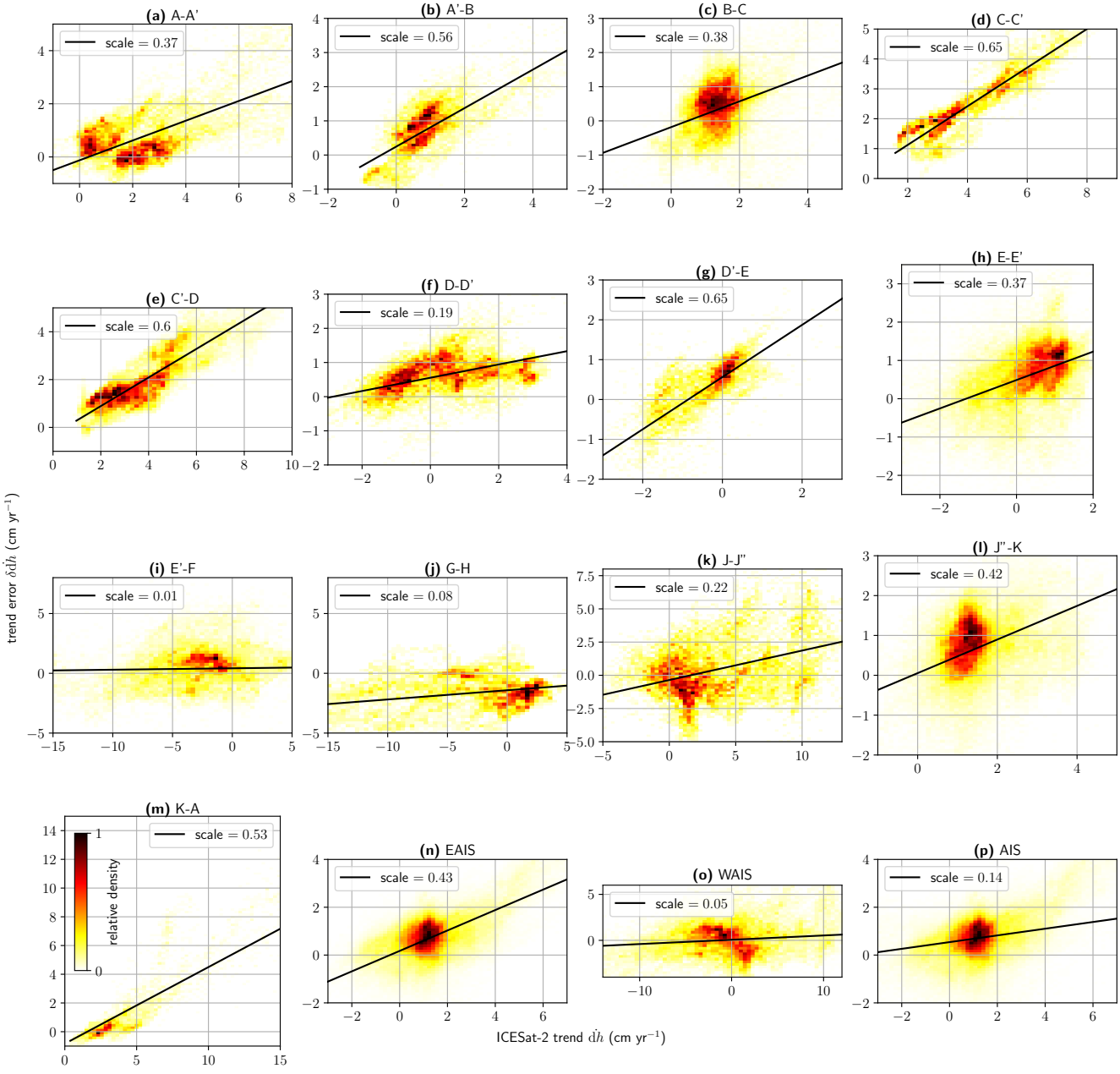

Figure S17. The ICESat-2 trend plotted against the CryoSat-2 trend error ($\delta\dot{dh}$) using OCOG10d for each basins. The black line shows the adjusted regression line (Eq. 14). Please note that the axis limits differ for each basin/panel.

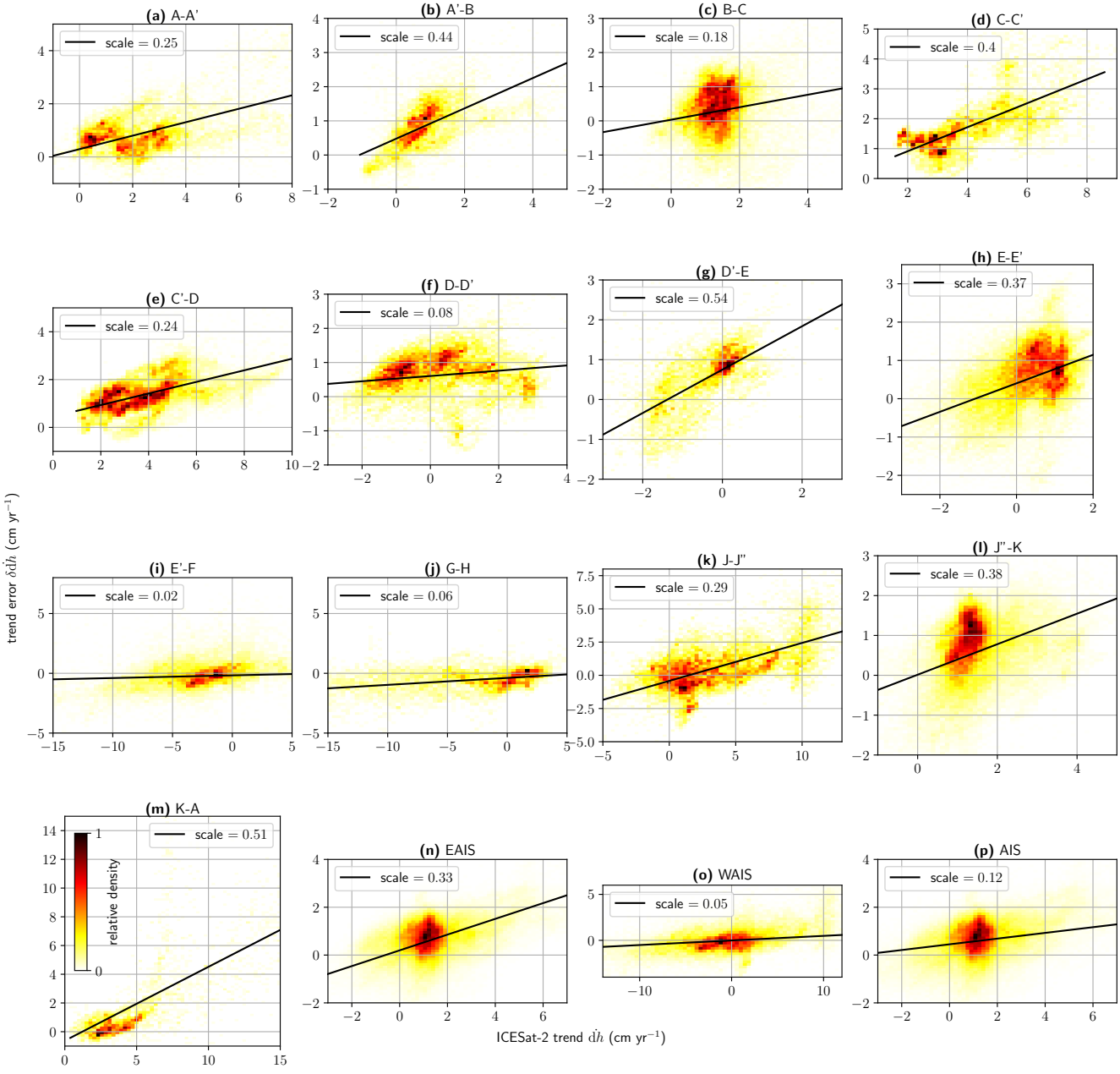

Figure S18. The ICESat-2 trend plotted against the CryoSat-2 trend error ($\delta\dot{dh}$) using AWI-ICENet1c for each basin. The black line shows the adjusted regression line (Eq. 14). Please note that the axis limits differ for each basin/panel.